Nano Energy 108 (2023) 108195

Contents lists available at ScienceDirect

Nano Energy

journal homepage: www.elsevier.com/locate/nanoen

Ultrahigh current output from triboelectric nanogenerators based on UIO-66 materials for electrochemical cathodic protection

Penghao Zhu [a,b], Zaka Ullah [c], Surong Zheng [b], Zairui Yang [b], Shiwei Yu [a], Shoupu Zhu [d], Liwei Liu [b], Aihua He [a], Cunguo Wang [a,*], Qi Li [b,*]

[a] Shandong Province Key Lab. of Olefin Catalysis and Polymerization, Qingdao University of Science and Technology, Qingdao 266042, China
[b] Key Laboratory of Nanodevices and Applications & Collaborative Innovation Center of Suzhou Nano Science and Technology, Suzhou Institute of Nano-Tech and Nano-Bionics, Chinese Academy of Sciences (CAS), Suzhou 215123, China
[c] Department of Physics, Division of Science and Technology, University of Education, Lahore 54770, Pakistan
[d] College of Energy Storage Technology, Shandong University of Science and Technology, Qingdao 266590, China

ARTICLE INFO

Keywords:
Triboelectric nanogenerator
Fermi level
External power supply
Metal corrosion

ABSTRACT

Metals are the basic and key components of most of the stuff present all around us in our living environment. The corrosion of these metals is a natural phenomenon which can be avoided through application of electrochemical cathodic protection. The triboelectric nanogenerator (TENG) is used to convert the environmental energy into electric energy. Unfortunately, the current output of TENG is always lower which limits its applications in protection of metal corrosion. In this work, we report the fabrication of efficient TENG based on UIO-66, UIO-66-NO_2 and UIO-66-NH_2, and use it as a power supply to construct a self-powered anticorrosion system for cathodic protection on carbon steel. The introduction of nitrate (-NO_2) and amine (-NH_2) groups change the Fermi level of the material, allowing the TENG to transfer more electrons during the contact. It is observed that the performance of TENG based on UIO materials is fruitful, with a maximum short-circuit current as 50.0 μA and a maximum power as 122.5 μW·cm^{-2}. In addition, dipping experiments and electrochemical measurements showed that the TENG is capable to offer notable cathodic protection to carbon steel. The demonstrated work introduces an efficient and cost-effective strategy for scavenging the mechanical energy from environment by employing the self-powered setup to effectually protect the metals from corrosion. The assembly of auspicious self-powered cathodic protection setup based on TENG offers a great potential for versatile applications in protection of metallic corrosion activities.

1. Introduction

The advancements in modern technologies have boosted the applications of metallic materials in our daily lives. The protection of metals from corrosion has attracted notable attentions of the researchers [1]. Generally, typical coatings and surface modifications are employed to protect the surfaces of such metals from corrosion [2–8]. However, the electrochemical cathodic protection is considered as one of the most efficient methods to protect the metals from corrosion. This approach is environment-friendly and offers prominent protective features. In this method, the electrons are injected into the metal to keep it at low potential all the time. This condition fundamentally protects the metal from corrosion [9]. However, an external power supply is required in this cathodic protection setup to deliver sufficient current output. This method has the disadvantages of high energy consumption and great environmental impact as it needs supporting power equipment connected to the grid to provide continuous power to protect the metals [10].

Researchers have demonstrated that the triboelectric nanogenerator (TENG) can be used as an external power source which can convert low-frequency environmental energy (the external wind energy, water energy and mechanical energy) to electrical energy without involving any other power source [11–21]. Unfortunately, the current output of TENG is lower which is limiting its applications in metal corrosion protection [22]. The charge density of friction layer in TENG is one of the crucial factors that controls the current output [12,23,24]. The charge-separation ability of the friction layer can be tuned through its physical or chemical modification and charge-transfer can be increased

* Corresponding authors.
E-mail addresses: wangcg@qust.edu.cn (C. Wang), qli2013@sinano.ac.cn (Q. Li).

https://doi.org/10.1016/j.nanoen.2023.108195
Received 26 November 2022; Received in revised form 23 December 2022; Accepted 7 January 2023
Available online 9 January 2023

during the contact between the friction layers which will enhance the output and hence performance of the TENG [24,25].

The fundamental factor which significantly affect the charge-separation is the relative Fermi level of the two friction layers. For the given two materials, the larger is the Fermi energy level difference, higher is the charge-transfer rate between the two materials during the contact process, and the higher is the surface charge density of the two materials, higher is the output performance of the TENG [24]. The demonstrated material is modified to purposefully regulate the Fermi level of the materials, and to increase the Fermi energy level difference between the two materials. In this way, the two output performances of TENG can be improved. It is well known that the Fermi level of semiconductor materials can be regulated by doping different types of impurities. If a donor impurity is added to an n-type semiconductor, its Fermi level shifts lower to the conduction band, while if a p-type semiconductor is added to an acceptor impurity, its Fermi level shifts to the top of the valence band. Based on this scheme, the Fermi level of the material is tuned.

In this work, we used UIO-66 as a matrix material and functionalized it with two groups -NO_2 and -NH_2 of different polarities. Here, N acts as an impurity to change the Fermi level of UIO-66. Three kinds of UIO-66 based materials (UIO-66, UIO-66-NO_2 and UIO-66-NH_2) are mixed with polyvinylidene fluoride (PVDF) to prepare UIO-66 @PVDF, UIO-NO_2 @PVDF and UIO-NH_2 @PVDF composite films as friction layers which are further used to fabricate UIO-based friction nanogenerator (UX-TENG). The test results show that the addition of the two groups effectively changes the Fermi level of UIO-66. The short-circuit current (I_{sc}) of UNH_2-TENG reaches to 50.0 μA with highest current density as 2.0 μA·cm^{-2} and power density as 122.5 μW·cm^{-2} which was enough to successfully light the number of LED lamps. In cathodic protection of external power supply, we used the UNH_2-TENG as an alternate power supply which slowed down the degree and rate of metal corrosion. The practice has proved that the UNH_2-TENG can offer diversity of auspicious applications particularly in metal corrosion protection.

2. Material and methods

2.1. Materials

Zirconium tetrachloride ($ZrCl_4$), N, N-dimethylformamide (DNF), 2-aminoterephthalic acid and 2-nitroterephthalic acid were supplied by Aladdin. Terephthalic acid (1, 4- benzenedicarboxylic acid: BDC), N, N-dimethylformamide (DMF), acetone and hydrochloric acid were provided by Sinopharm Chemical Reagent Co., Ltd. Whereas, the PVDF was purchased from Aldrich Chemicals. All the materials were used without any pre-treatment.

2.2. Preparation of UIO-66 and its derivatives

Hydrothermal method was employed for the assembly of UIO-66. Zirconium tetrachloride ($ZrCl_4$, 349.56 mg, 1.5 mmol), terephthalic acid (250 mg, 1.5 mmol), hydrochloric acid (HCl, 6 M, 7 ml) and N, N-dimethylformamide (DMF, 50 ml) were mixed together in a Teflon-lined stainless-steel container. The materials were placed in a reactor for drying up to 24 h at 120ºC. During the centrifugation, the precipitated products were obtained which were washed twice with N, N-dimethylformamide and deionized water. The obtained products were dried in oven at 60ºC. The preparation method of UIO-66-NO_2 and UIO-66-NH_2 was the same as that of UIO-66 except 2-nitroterephthalic acid (316.70 mg, 1.5 mmol) and 2-amino terephthalic acid (271.73 mg, 1.5 mmol) were used instead of benzoic acid.

2.3. Preparation of UIO@PVDF composite film

A solution of PVDF (3.75 g), acetone (12.75 g) and N, N-dimethylformamide (DNF, 8.5 g) was prepared in 100 ml beaker. Later, UIO-66 with different concentrations (wt%=5%, 10%, 15%) was dispersed into the solution. The stirring of solution was performed at 60ºC for 2 h to dissolve the PVDF completely. Afterward, the solution was cooled down to the room temperature which assembled UIO-66 @PVDF. Polyimide (PI) films were cleaned with acetone and anhydrous ethanol for 30 min through ultrasonication. The UIO-66 @PVDF slurry was rotated on PI films and dried in an oven at 40ºC for 12 h. Finally, the film was cut into pieces of 5 × 5 cm^2. The final product was the composite film of UIO-66 @PVDF/PI. UIO-NO_2 @PVDF/PI and UIO-NH_2 @PVDF/PI were obtained through similar fashion.

2.4. Fabrication of UX-TENG

Polymethyl methacrylate (PMMA) was used as a supporting plate, 3 M glue as the buffer layer and a copper foil and then UIO-66 @PVDF/PI composite film were placed on it. Copper foil was used as an induction electrode for TENG and UIO-66 @PVDF acted as a friction layer. The second electrode also used PMMA as a supporting layer, 3 M glue as the buffer layer, copper foil as an induction electrode, and pure PVDF as a friction layer. Finally, UIO-66 @PVDF and pure PVDF based TENG was fabricated. TENG with friction layer of UIO-66 @PVDF-PVDF, UIO-NO_2 @PVDF-PVDF and UIO-NH_2 @PVDF-PVDF were assembled using the similar approach. The charge-separation and energy conversion of UX-TENG were caused by the contact charge between the composite membrane and pure PVDF membrane. The effective area of the device was 5 × 5 cm^2.

X-ray diffraction (XRD) analysis was employed to study the crystal structures of prepared materials, using the Bruker D8 Advance which works with Cu Kα irradiation (λ = 1.5406 Å), in the 2θ range of 5–90°. The composite film was characterized for its molecular structure using the Fourier transform infrared (FTIR) spectroscopy (Thermo Scientific Nicolet Is20). Scanning electron microscope (SEM: Hitachi S-4800 Japan) was used to observe the surface features of UIO-66 @PVDF, UIO-NO_2 @PVDF and UIO-NH_2 @PVDF composite films. The open circuit voltage (V_{oc}) and short circuit current of TENG were measured by Keithley 2400 source meter and electrochemical workstation (Shanghai Chenhua CHI760).

3. Results and discussion

3.1. Morphological characterization of UIO-66 and its derivatives

The structure of UIO-66, UIO-66-NO_2 and UIO-66-NH_2 crystals was simulated as shown in Fig. 1a. UIO-66 crystal consists of zirconium oxide complex which forms the metal nodes. The nodes are arranged and assembled into bridged structure with the help of terephthalic acid linkers. In $Zr_6O_4(OH)_4$ node, six Zr^{4+} ions get connected with four oxygen or hydroxyl atoms and form octahedral geometry. It was found that the crystal structure of UIO-66 did not change after the introduction of -NO_2 and -NH_2 groups and it sustains its regular octahedral structure.

In order to further verify the influence of -NO_2 and -NH_2 groups on the crystal structure of UIO-66 and its derivatives, their XRD and FTIR spectroscopy analyses were conducted. The simulated and recorded XRD patterns of UIO-66, UIO-66-NO_2 and UIO-66-NH_2 metal-organic framework (MOF) particles (Fig. 1b) are consistent with each other and show octahedral structure. The diffraction peaks (111), (002) and (006) found respectively at 2θ values 7.3, 8.5 and 25.8° are associated with space group cubic Fm-3 m. FTIR spectra of prepared samples are shown in Fig. 1c. In UIO-66, the stretching and bending vibration absorption peaks for -OH are detected at 3201 and 1396 cm^{-1}. The absorption peaks at 1153 and 1018 cm^{-1} are ascribed to C-O stretching vibrations which confirm the presence of carboxylate groups. Whereas, the peaks observed at 1587 and 1507 cm^{-1} are credited to C═C stretching mode which arose from sp^2 carbon skeleton. Moreover, the characteristic bands at 745 and 653 cm^{-1} correspond to C-H vibrations of the organic compounds.

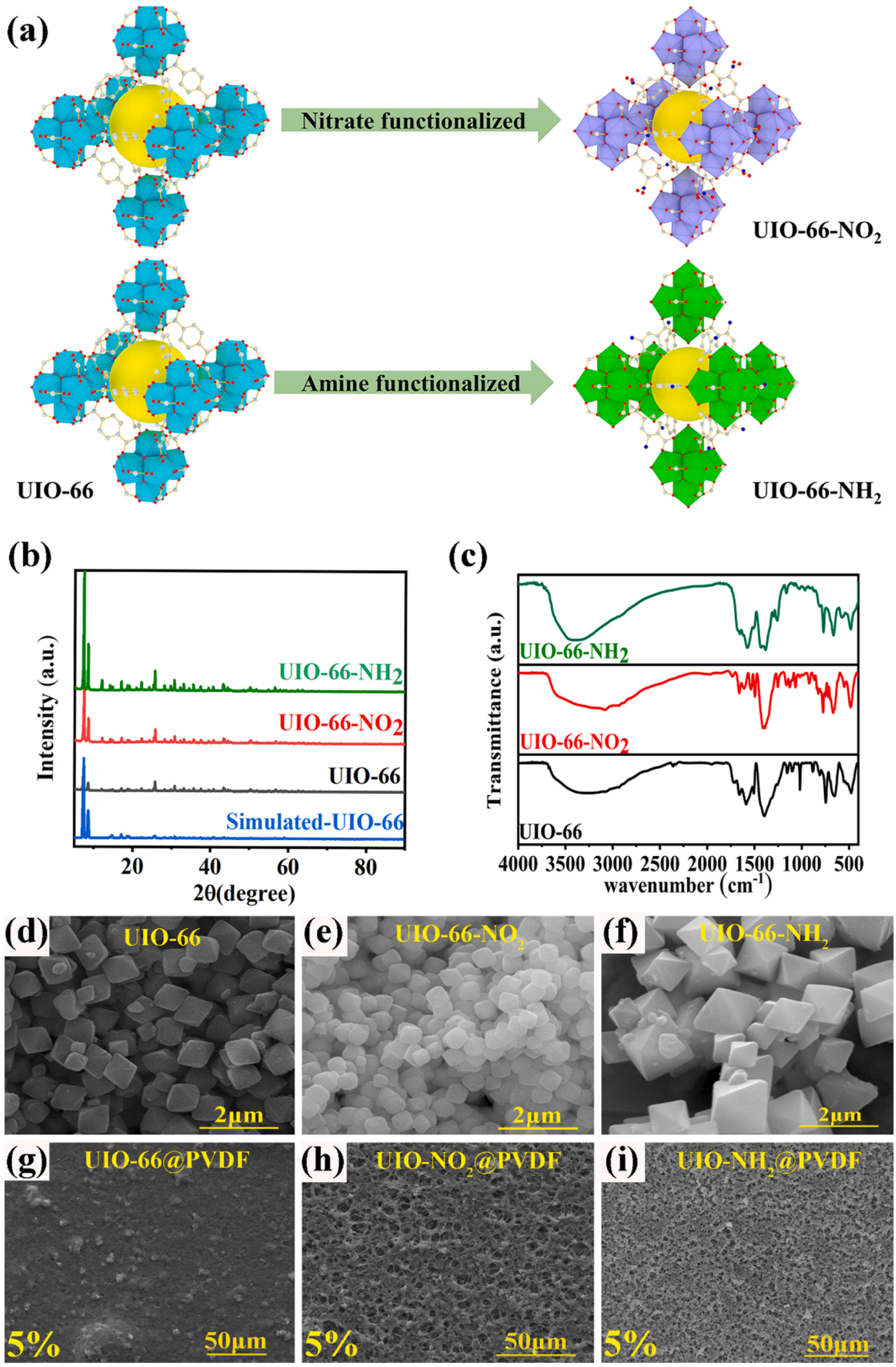

Fig. 1. Structural and morphological characterizations of UIO-66 and its derivatives. (a) Simulated and (b) recorded XRD patterns of UIO-66 and its derivatives. (c) FTIR spectra of UIO-66 and its derivatives. SEM images of (d) UIO-66, (e) UIO-66-NO_2, (f) UIO-66-NH_2, (g) UIO-66 @PVDF, (h) UIO-NO_2 @PVDF and (i) UIO-NH_2 @PVDF (UIO as 5 wt%) composite films.

FTIR spectra peaks at 920, 773 and 1541 cm^{-1} for UIO-66-NO_2 are attributed to C-N bond which joins the nitro group with aromatic group. The peaks at 3048, 1659 and 1253 cm^{-1} belong to -OH stretching vibrations, -C═O stretching vibrations and bending vibrations, respectively. In UIO-66-NH_2, the absorption peaks at 3411, 1430 and 1383 cm^{-1} are attributed to stretching vibrations of N-H bond. These further indicate the presence of N-H bond in aromatic ring. Moreover, in order to further illustrate the successful synthesis of the materials, SEM tests of the three materials were also conducted (Fig. 1d-f). SEM micrographs of UIO-66, UIO-66-NH_2 and UIO-66-NO_2 MOF particles further confirm their morphology as octahedral. The crystal structure of UIO-66-NO_2 is relatively fuzzy as compared to that of UIO-66 and UIO-66-NH_2. It can be attributed to the volume of -NO_2 group which is larger than that of -NH_2 group. It evidences that the addition of -NO_2 and -NH_2 groups did not affect the crystal structure of UI-66, and these are efficiently attached to it.

The prepared UIO samples (UIO-66, UIO-66-NO_2 and UIO-66-NH_2) are doped with PVDF in three proportions (wt% as 5%, 10% and 15%, respectively), and spin coating approach is used to prepare the UIO@PVDF composite membranes (UIO-66 @PVDF, UIO-NO_2 @PVDF

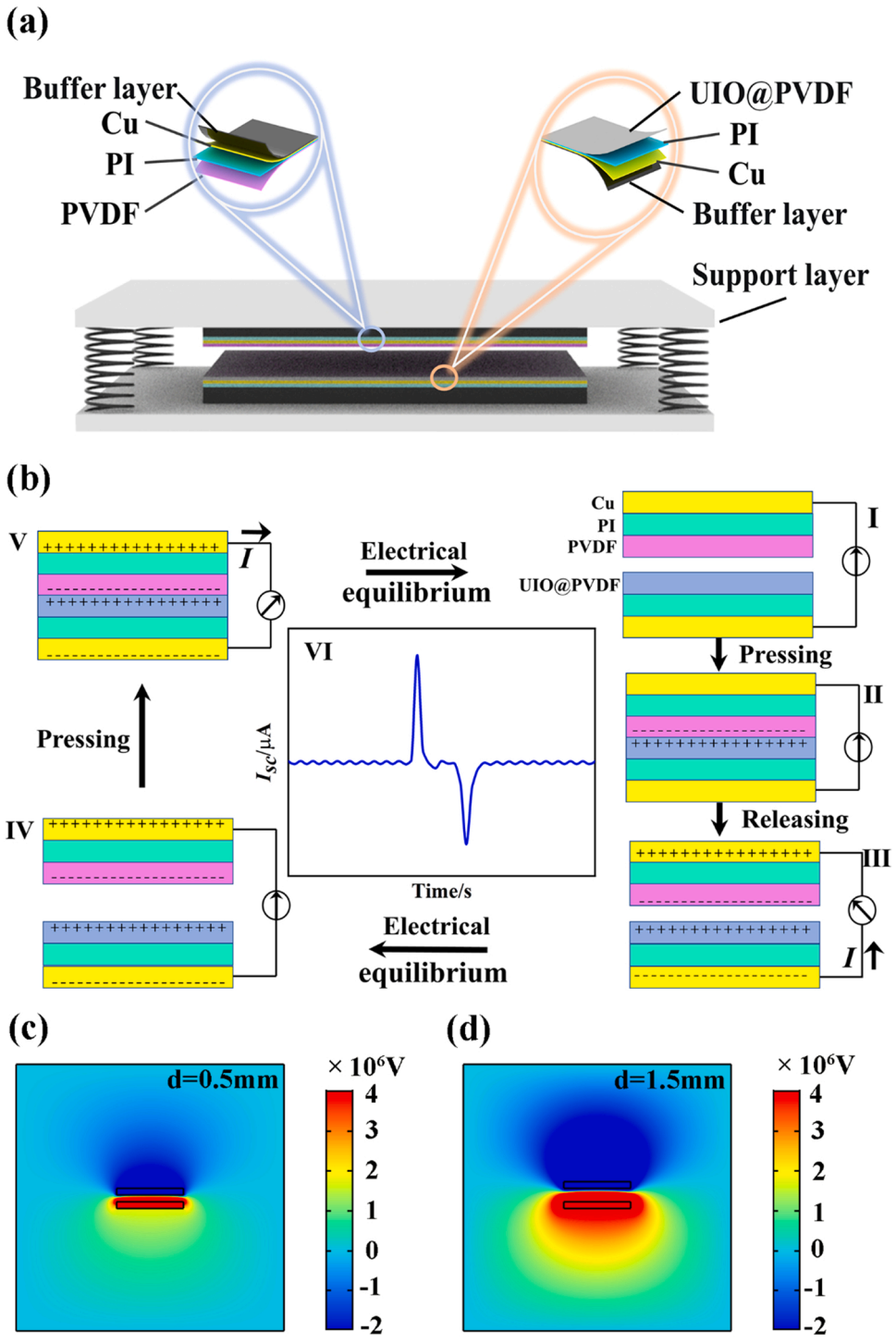

Fig. 2. (a) Schematic showing the 3D structure of UX-TENG. (b) Working principle and short circuit current output of UX-TENG. (c, d) COMSOL simulation for electrical potential changes in UX-TENG during the application of force which changes the distance between the two layers as (c) x = 0.5 mm and (d) x = 1.5 mm.

and UIO-NH_2 @PVDF). Fig. 1g-i shows the SEM images of PVDF doped (wt%=5%) UIO materials. As compared to pure PVDF membrane (Supporting Information, Fig. S1), the UIO@PVDF composite films show obvious granular morphology which indicates that the mixing of UIO and PVDF was typically a physical doping process. The surface of UIO-NO_2 @PVDF and UIO-NH_2 @PVDF composites is more porous than that of UIO-66 @PVDF which can be attributed to additions of -NO_2 and -NH_2 groups. These groups are highly hydrophilic and accelerate the exchange rate of solvent and non-solvent in the process of film formation which further leads to the formation of a number of pores on the surface of membranes [26]. The increase in doping concentration in UIO materials increases the agglomeration in UIO-66-NO_2 and UIO-66-NH_2 which further leads to the decrease in number of pores on the surface of composite films (Supporting Information, Fig. S2).

3.2. Structure and working principle of UX-TENG

Fig. 2a shows the 3D schematic diagram of demonstrated UX-TENG. Here, UIO@PVDF composite film and pure PVDF film act as friction layers and these are attached to the respective PI film. On outer side of the PI film, a layer of copper foil is attached as an inductive electrode, 3 M glue is used as a buffer material, and acrylic plate is used as a supporting layer. These are combined to assemble the UX-TENG. The UX-TENG uses a contact-separation operating mode. Its working principle relies on coupling effect which is produced between the contact electrification and electrostatic induction.

Fig. 2b I-V elucidates that how the charges are generated and transferred between the UIO@PVDF and PVDF interacting surfaces. Fig. 2b I show the electrical status of two surfaces. In start, as there is no force, there is no charge generation in the friction layers. The contact is developed between the two surfaces as the external force is applied, and opposite charges of same magnitude are produced in the two surfaces (Fig. 2b II). The electrons are transferred from UIO@PVDF to PVDF owing to triboelectric effect of active materials. This process makes UIO as positively charged and PVDF as negatively charged. The two layers try to restore their initial electrical states as the external force is released. This scheme develops an electric potential difference in the circuit which causes the flow of electrons from PVDF to UIO@PVDF electrode (Fig. 2b III). This flow of charges produces the half cycle of output signal. The potential difference is maximum when the external force is completely removed, as shown in Fig. 2b IV. However, as the external force is reapplied, the TENG gets compressed and developed potential difference is decreased which causes the electrons to flow in the reverse direction. Hence, a peak in reverse direction of output signal is observed (Fig. 2b V). As the two layers get neutralized, the equilibrium state in TENG is obtained. As the periodic force is applied and device gets compressed and stretched, the developed potential between the two electrodes increases and decreases periodically which generates the alternating current in the external circuit (Fig. 2b VI).

In contact mode operation, output open circuit voltage (V_{oc}) and short circuit current (I_{sc}) can be calculated using the following Eq. (1) and eq. (2), respectively:

$$V_{oc} = \frac{\sigma_o x(t)}{\varepsilon_o} \tag{1}$$

$$I_{sc} = \frac{\sigma_o S v(t)}{(d_o + x(t))^2} \tag{2}$$

Here, σ_o denotes triboelectric charge density at the surface, $x(t)$ gives distance between the two friction layers, and ε_o informs about air permittivity. To elucidate the operation of TENG, the potential distribution was simulated using the COMSOL multi-physics software, as presented in Fig. 2c-d. The simulated potential distribution of TENG is consistent with Eq. (1) and eq. (2). Moreover, the amount of charge transferred to electrode is increased with increase in distance between the two electrodes. In addition, according to Eq. (1) and eq. (2), under the conditions of same dielectric constant, separation distance and contact area, charge density σ_o at the surface of friction layer is the determining factor of I_{sc} and V_{oc}. When σ_o is larger, I_{sc} and V_{oc} are greater.

3.3. Output performance of the UX-TENG

For practical applications, the stability of the TENG is rather important for continuous energy harvesting from the ambient environment. It is necessary to study the relationship between the output signals and the mechanical energies harvested from the irregular conditions. Here, we utilized classic periodic impacts to characterize the output performance of the UNH$_2$-TENG. It can be clearly seen that I_{sc} becomes larger as the frequency is increased (Supporting Information, Fig. S3). When the frequency is above 9 Hz, the output reaches the maximum values. Hence, this work was carried out at the frequency of 9 Hz in the subsequent experiments.

UIO@PVDF composite and pure PVDF films are used as two friction layers and UX-TENGs are fabricated. The performance of UX-TENGs is evaluated by testing their electrical output efficiency (Fig. 3a-c). When TENG is fabricated using PVDF-PVDF as friction layers, a small amount of 0.87 μA current output is received. There could be a smaller charge transfer when two identical materials contact each other. Whereas, UX-TENG based on UIO@PVDF composite and pure PVDF membranes exhibit maximum electrical output performance; it is recorded as 30.0, 40.7 and 50.0 μA for U66-TENG, UNO$_2$-TENG and UNH$_2$-TENG, respectively. Moreover, when different proportions as 5 wt%, 10 wt% and 15 wt% of UIO-66 are doped in PVDF, the output of U66-TENG is reached to 16.5, 17.4 and 30.0 μA, respectively. In addition, I_{sc} of UNO$_2$-TENG has low short circuit current than NH$_2$-TENG. This is attributed to electronegativity of oxygen in -NO_2 which is greater than that of nitrogen, and the charge in the nitro group which is attracted by oxygen and results in decrease the number of free charges. Where in -NH_2, N has highest electronegativity. The number of free charges that -NH_2 can provide by guiding band is greater than -NO_2. Therefore, the power output property of UNH$_2$-TENG is greater than that of UNO$_2$-TENG.

As the concentration of UIO-66-NO_2 is doped as 5 wt%, 10 wt% and 15 wt%, the output of UNO$_2$-TENG is also increased to 27.0, 38.1 and 40.7 μA, respectively. It is obvious that the increase in current output of UNO$_2$-TENG is due to the addition of -NO_2 group in UIO-66. Similarly, by introducing -NH_2 group into UIO-66, the current output of the fabricated UNH$_2$-TENG with UIO-66 as 5 wt%, 10 wt% and 15 wt% is respectively enhanced to 36.0, 42.8 and 50.0μA. It was much higher than that of the same proportion of U66-TENG. The results evidence that -NO_2 and -NH_2 play a key role in promotion of heterogeneous charge separation between frictional layers and enhancing the overall performance of TENG. At the same time, the open circuit voltage (V_{oc}) of UNH$_2$-TENG, is up to 210 V (Supporting Information, Fig. S4). It can be concluded that -NO_2 and -NH_2 play the crucial role in boosting the electrical output of TENG.

The functional groups -NO_2 and -NH_2 have different polarities and TENGs were fabricated using the UIO-NO_2 @PVDF and UIO-NH_2 @PVDF composite films as two frictional layers. In these devices, the maximum value of I_{sc} was found as 10μA (Supporting Information, Fig. S5) which was much lower than I_{sc} of TENG based on composite and pure PVDF membranes. This indicates that the two groups -NO_2 and -NH_2 with different polarity may have the same modification effects on UIO-66. The UIO-66-NO_2 and UIO-66-NH_2 deliver a smaller I_{sc} when these act as friction layers in TENG. Consequently, the polarity of the group is not the key factor affecting the overall performance of the TENG.

In order to determine the unidirectional current, the rectifier bridge was connected with UNH$_2$-TENG (15 wt%); the connection setup in given in Supporting Information Fig. S6; the rend of I_{sc} can be observed in Fig. 3d. Charge density σ is also one of the important indicators to measure the output performance of TENG. Fig. S7 in Supporting

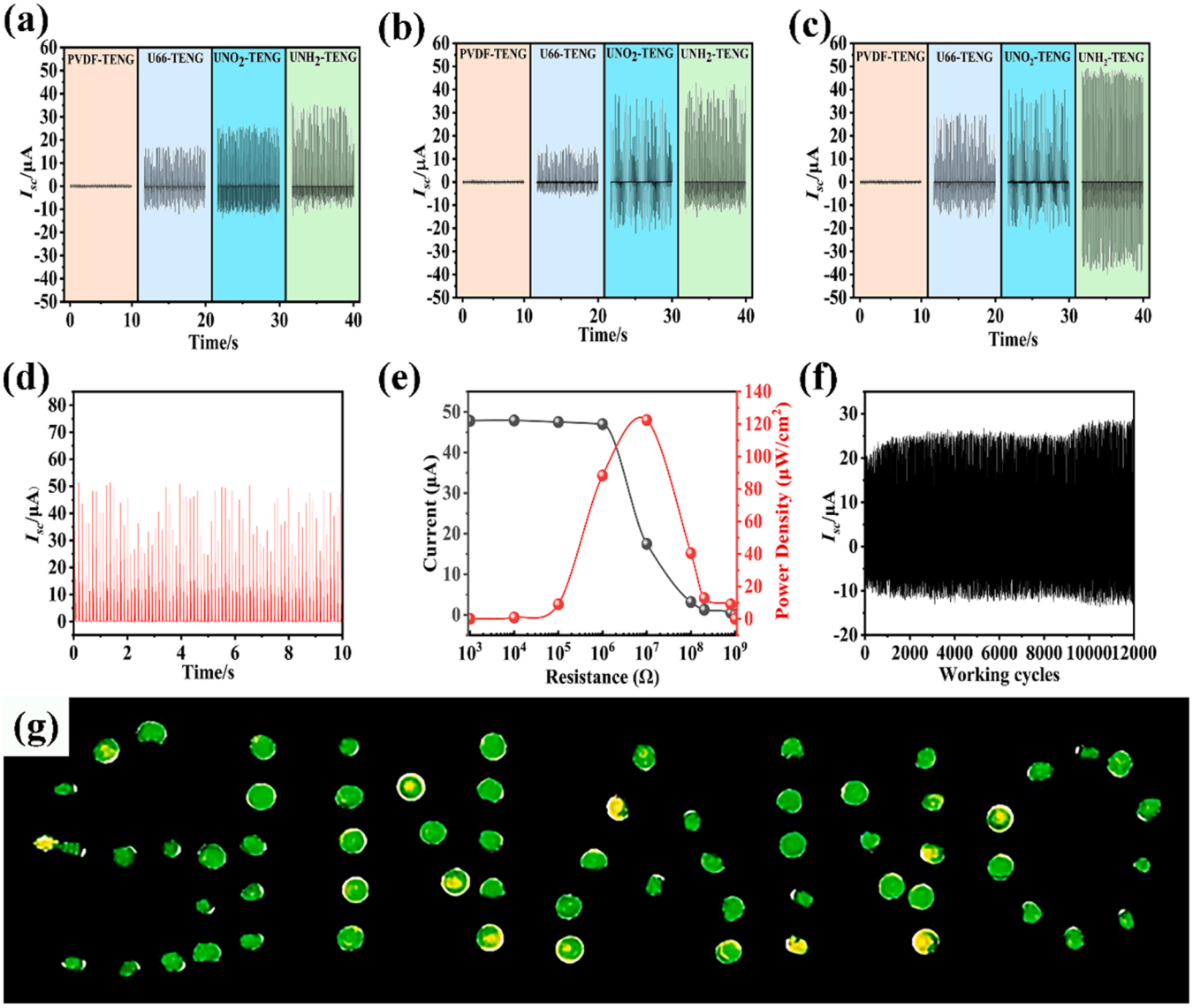

Fig. 3. I_{sc} output performance of UX-TENG and PVDF-TENG with (a) 5 wt%, (b) 10 wt%, and (c) 15 wt% of UIO-66. (d) Output response of UNH_2-TENG. (e) The load and current of external circuit in UNH_2-TENG for corresponding power. (f) Durability of UNH_2-TENG for 12,000 cycles. (g) TENG lighting the commercial LED lamps.

Information shows the charge density corresponding to Fig. 3d, which is up to 60.79 μC m^{-2}. Fig. 3e shows the dependence of I_{sc} and corresponding power on external load resistance. Due to ohmic loss, I_{sc} decreases gradually with increasing resistance, and the maximum power is determined as 122.5μWcm^{-2} when the load resistance is 10 MΩ. The durability test was also carried out which lasted for about 12,000 cycles (Fig. 3f). The I_{sc} remained comparatively stable after 12,000 successive cycles, indicating that the notable durability of UNH_2-TENG offers valuable potential for its auspicious applications. In order to further verify the practicability of UNH_2-TENG as a power source, it was successfully used to light the commercial LED lamp (Fig. 3g and video 1), suggesting the development prospect of UNH_2-TENG in practical applications.

Supplementary material related to this article can be found online at doi:10.1016/j.nanoen.2023.108195.

The energy collection and storage are two closely related processes in energy applications, so the charging capacity of TENG is also one of the criteria to measure its practicability [27]. In order to verify the charging ability of the UNH_2-TENG, a 10μF capacitor was charged using the UNH_2-TENG. Fig. S8a in Supporting Information depicts the charging of a 10μF capacitor to 10 V, with gradually increasing the charging voltage as a function of time. Fig. S8b shows the charging status of the UNH_2-TENG in one cycle. It can be seen that the charging voltage reaches to 2.0 V and the charge transfer to 20μC in one cycle.

The performance evaluation parameters of various TENGs reported in literature have been compared with the demonstrated ones in Table 1. These parameters include the friction layer materials, effective contact area, short-circuit current and short-circuit current per unit area. The short-circuit current in UNH_2-TENG was observed as 50.0 μA, and the

Table 1
Electrical output performance of several TENGs.

TENG	Size (cm)	I_{sc} (μA)	I_{sc} (μA·cm^{-2})	Reference
PDMS-Cu	3 × 3	3.5	0.389	[28]
PDMS-Al	3 × 3	3.8	0.422	[29]
PDMS-CNTs	2.5 × 2.5	0.18	0.029	[30]
PTFE-Al	4 × 4	6.7	0.419	[31]
PBOA-PEO	5 × 5	2	0.080	[32]
ZIF-7-PI	2.5 × 2.5	1.1	0.176	[33]
UIO-66 @PVDF-PVDF	**5 × 5**	**30**	**1.200**	**This work**
UIO-NO_2 @PVDF-PVDF	**5 × 5**	**40.7**	**1.628**	**This work**
UIO-NH_2 @PVDF-PVDF	**5 × 5**	**50.0**	**2.000**	**This work**

short-circuit current per unit area as 2.00 μAcm^{-2} which are about 4 times higher than of others devices.

In order to clarify the attribution of high current, Fermi level is one of the key factors to be examined. It affects the charge transfer during the establishment of contact between the two materials. Larger is the difference of Fermi levels between the dissimilar materials, greater is the charge transfer. Work function can directly reflect the difference of Fermi levels of different materials, as shown in Fig. 4a. Whereas, W_A and W_B are the work functions and E_{FA} and E_{FB} are the Fermi levels of two materials; E_{FA1} and E_{FB2} are Fermi levels after charge transfer between

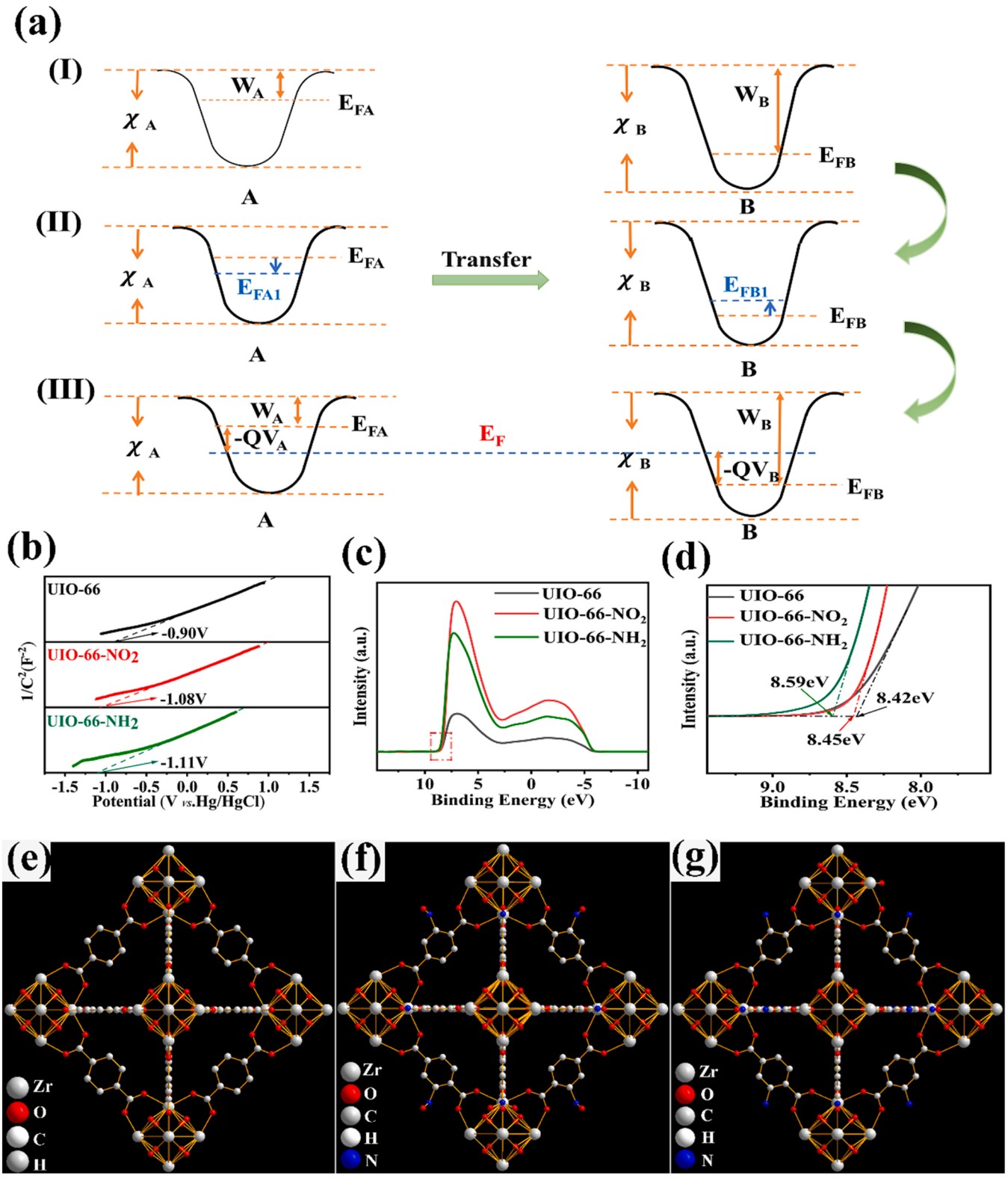

Fig. 4. (a) Schematic diagram showing the charge transfer mechanism during contact of dissimilar materials. (b) Mott-Schottky curves and (c) UPS profiles of UIO-66, UIO-66-NO_2 and UIO-66-NH_2. (d) Enlarged view of selected area of plot in (c). (e-f) Schematic diagram of UIO-66, UIO-66-NO_2 and UIO-66-NH_2 crystal structure.

the two materials; E_F is Fermi level in equilibrium between the chemical potentials of the two materials; $-QV_A$ and $-QV_B$ are electrostatic potential energies generated after the charge transfer between the two materials.

As the two different heterogeneous materials A and B come in contact with each other (Fig. 4a-I), electron transfer can take place from higher chemical potential to lower chemical potential (Fig. 4a-II). After the charge transfer, side A becomes positively charged and side B becomes negatively charged. The electrostatic potential generated on the surface of the material should be:

$V_A > 0$ and $V_B < 0$.

In this scenario, the electrons in the two materials A and B will generate additional electrostatic potential energy, which should be:

$-Q \cdot V_A < 0$ and $-Q \cdot V_B > 0$.

Here, Q represents the charge transferred between the two materials. From the energy level diagram (Fig. 4a-III), the whole energy level $-QV_A$ of A material decreases and the energy level $-QV_B$ of B material increases, leading to the flattening of Fermi levels of both materials. Once the Fermi levels of two materials are same or close to each other, the electronic chemical potentials of the two materials are equal, and there is no further large-scale transfer of electrons.

The two materials compensate for the difference in their Fermi levels by generating the electrostatic potential energy difference, thus bringing the electrons to the statistical equilibrium. It can be observed that the larger is the difference between the Fermi levels of two materials, the more electrons tend to transfer and more electrostatic potential energy is generated to compensate the difference. The introduction of $-NO_2$ and $-NH_2$ groups into UIO-66 change the Fermi level of UIO-66 and increase the charge transfer between the two materials which notably improves the performance of TENG.

The Mot-Schottky (M-S) curves of UIO-66, UIO-66-NO_2 and UIO-66-NH_2 confirm the above suggestions. The slope on straight part of M-S curve for UIO-66 and its derivatives is positive (Fig. 4b), indicating that all three materials are n-type semiconductor. Since the flat band potential is exactly aligned with the Fermi level energy of semiconductor electrode which means E_F=E_{FB} (E_F is the Fermi level and E_{FB} is flat band potential level), hence the corresponding Fermi level of the material can be calculated from flat band potential obtained from the M-S curve [34]. The values of flat band potential of UIO-66, UIO-66-NO_2 and UIO-66-NH_2 are − 0.90, − 1.08 and − 1.11 V, respectively. According to Eq. (3) and eq. (4), their electrochemical scales are transformed into solid state physical scales to obtain the corresponding Fermi levels:

$$E\ (vs{\cdot}SHE)^{\theta} = E\ (vs{\cdot}SCE)^{\theta} + E\ (vs{\cdot}SCE) \quad (3)$$

$$E_{ps}(eV) = E\ (vs{\cdot}SHE)^{\theta} - 4{\cdot}6\ eV \quad (4)$$

Whereas, E (vs. SHE)$^{\theta}$ is the standard hydrogen electrode potential (0.2415 V), E (vs. SCE)$^{\theta}$ is the standard saturated calomel electrode potential, E (vs. SCE) is the test value and E_{ps}(eV) is the physical energy level scale of solid state. The E_{ps}(eV) of UIO-66, UIO-66-NO_2 and UIO-66-NH_2 are calculated as − 3.94, − 3.79 and − 3.73 eV, respectively. It is observed that when $-NO_2$ and $-NH_2$ groups are introduced into UIO-66, the Fermi level of UIO-66 changes and the conduction band direction shifts gradually, which verifies that the N atom in the group acts as a donor impurity and the conduction band provides electrons, leading to the bottom shift of the Fermi level conduction band. The $-NO_2$ and $-NH_2$ groups are located in the gap between the lattice atoms, as shown in Fig. 4e-g. There is a lone pair of electrons in N atom which can be transferred to the conduction band of the material. Therefore, N plays the role of donor impurity in UIO-66 crystal and changes the Fermi energy level of UIO-66.

In addition, the relative change in work function of three materials indicates the addition of functional groups and their influence on Fermi level of the materials. Fig. 4c-d shows the ultraviolet photoelectron spectroscopy (UPS) results of the three materials, where Fig. 4d is the enlarged view of plot area highlighted in Fig. 4c. The work function of UIO-66 was calculated to be 3.80 eV. After the introduction of $-NO_2$ and $-NH_2$, the work function of UIO-66-NO_2 and UIO-66-NH_2 were determined respectively as 3.77 and 3.63 eV. As compared to UIO-66, the work function of its derivatives reduced up to some extent, indicating that the binding ability of the materials to electrons is reduced and the ability to conduct the electrons is enhanced. During the contact development with pure PVDF, the difference of work function of UIO-NO_2 @PVDF and UIO-NH_2 @PVDF with pure PVDF is increased accordingly.

3.4. Application of UNH2-TENG in metal corrosion protection

The setup designed for cathodic corrosion protection based on UNH_2-TENG is sketched Fig. 5a. The system is linked with rectification bridge where its negative terminal is directly connected with carbon steel and positive terminal with graphite electrode. A linear mechanical motor was employed to drive it. Electrochemical polarization profiles are recorded to study the corrosion behavior. The corrosion current (I_{corr}) and corrosion potential (E_{corr}) are measured by extrapolating the linear portion of curves in Tafel plots for cathodic and anodic branches. A negative shift in E_{corr} is observed in cathodic protection system which evidences the enhanced cathodic protection for corrosion. Fig. 5b shows the polarization response of carbon steel connected with and without UNH_2-TENG. The values of I_{corr}, E_{corr}, anodic Tafel slope (β_a) and cathodic Tafel slope (β_c) are determined from polarization results (Supporting Information, Table S1). When the system is connected with cathodic protection setup powered by UNH_2-TENG, the carbon steel gives negative shift in E_{corr}. Meanwhile, there is a small increase in I_{corr} due to injection of electrons generated in UNH_2-TENG. This enhances the electrochemical activity on the surface of carbon steel. The polarization results suggest that by providing sufficient electrons, the cathodic protection system with UNH_2-TENG power source can efficiently protect the surface of carbon steel from corrosion.

Electrochemical impedance spectroscopy (EIS) is one of the important methods to study the efficiency of cathodic protection. Fig. 5c shows the impedance spectra of cathodic protection system with and without UNH_2-TENG. The spectra consist of an arc and a tail line, where the arc informs about charge transfer resistance (R_{ct}). The smaller is the semicircle radius, the lower is the reaction resistance. The electrochemical reaction has more tendency to take place on the surface of metal which will lead to a few or no corrosion points on the carbon steel surface. The semicircle radius of charge transfer impedance when connected with the UNH_2-TENG protection setup, is smaller than that of when did not connect with UNH_2-TENG protection setup, which clearly indicates the efficient role of TENG for cathodic protection. In order to show the function of UNH_2-TENG as external power source more proficiently, the equivalent circuit analysis of carbon steel with and without UNH_2-TENG was employed as per EIS data (Fig. 5d). The R_{ct} value representing the charge transfer resistance in equivalent circuit of carbon steel was 281.1 Ω when it was not connected with UNH_2-TENG, and was decreased to 237.9 Ω when it was connected with UNH_2-TENG. This further indicates the role of UNH_2-TENG in protection of metal from corrosion (Supporting Information, Table S2).

To investigate the corrosion of carbon steel under different conditions, three carbon steels were tested. First was not connected to TENG, second was connected to U66-TENG and third was connected to UNH_2-TENG. These were immersed in 3.5 wt% NaCl solution for 2, 4 and 6 h. The results show that the surface of carbon steel without TENG gets completely covered by rust patches just after 2 h of immersion, and the rust deteriorates with the extension of immersion time (Fig. 5d). In case of carbon steel connected with U66-TENG, a small current produces a small number of corrosion pits on the surface of carbon steel after 2 h of immersion. The number of corrosion pits are increased after immersion of 4 h, and the corrosion of carbon steel is further intensified after 6 h (I_{sc} trends of U66-TENG after rectification are shown in Supporting Information, Fig. S9).

On the other hand, as the carbon steel is connected with UNH_2-TENG, no obvious corrosion phenomenon is observed upon soaking the

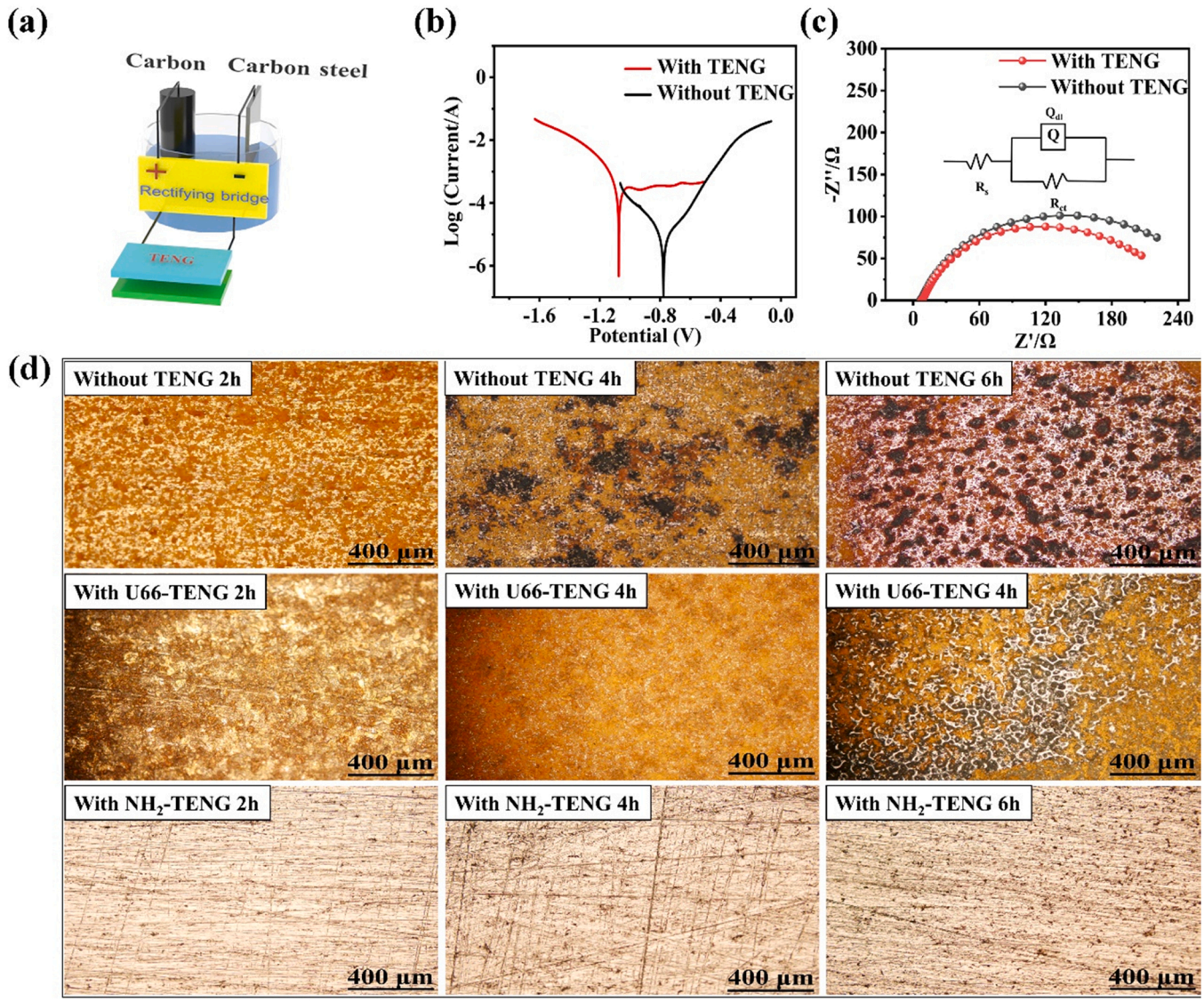

Fig. 5. Schematic diagram for cathodic protection through electrochemical activity. (a) Cathodic protection system. (b) Tafel curves for carbon steel recorded with setup in the absence and presence of TENG. (c) EIS profiles for carbon steel and equivalent circuit diagrams for connected and disconnected TENG. (d) Corrosion response of carbon steel connected to different versions of TENG.

carbon steel in solution for 2 h. Even when the soaking time is extended up to 6 h, very few corrosion pits are produced on the surface of carbon steel. Thus, UNH_2-TENG effectively protects the carbon steel from corrosion. It is suggested that the electrons generated by TENG pass through the connection lines and eventually enter into the carbon steel to provide the cathodic protection. As the current output of UNH_2-TENG is greater than U66-TENG and UNO_2-TENG, the corrosion protection efficiency of UNH_2-TENG is greater for carbon steel as compared to other two setups. This also shows the importance of high current output for metal corrosion protection system. In this regard, the UNH_2-TENG power cathodic protection system is an important approach of electrochemical corrosion control. Generally, the oxidation reaction takes place at anode which suppresses the corrosion of cathodic protected carbon steel.

In a cathodic protection system, the open circuit potential (OCP) drop which is an important parameter, has been used to evaluate the cathodic protection efficiency. A more negative OCP shift indicates a better cathodic protection effect. As shown in Supporting Information Fig. S10, the OCP variation of carbon steel with and without the UNH_2-TENG (15 wt%) are measured in a three-electrode system with a saturated calomel electrode (SCE) as the reference electrode and graphite as the counter electrode in a 3.5 wt% NaCl solution. The OCP of the carbon steel without the TENG is about − 0.66 V (vs. SCE) and shifts sharply to − 0.99 V (vs. SCE) after being connected to the cathodic protection system powered by the TENG. Therefore, the OCP shifts negatively by about 330 mV, indicating that the carbon steel is under effective cathodic protection. It is noteworthy that when the UNH_2-TENG is removed, the OCP shifts positively and recovers to the position near to the original value. The periodic change of the OCP reflects the high repeatability of the UNH_2-TENG for powering the cathodic protection system.

4. Conclusions

In summary, UX-TENG devices are fabricated and employed for electrochemical cathodic protection through harvesting the mechanical energy from environment in which the metallic stuff is used. The introduction of $-NO_2$ and $-NH_2$ groups changed the Fermi level of the material and increased the amount of charge transfer, which provided an effective idea for modification of material for TENG friction layer. The UX-TENG delivered maximum peak value of I_{sc} as 50.0 μA and power density as 122.5μW·cm^{-2}. The cathodic corrosion protection

system with UNH_2-TENG power source was built to protect carbon steel against corrosion. The immersion results show that the carbon steel connected with UNH_2-TENG did not accept the corrosion in 3.5 wt% NaCl solution for 2 h. Furthermore, the electrochemical polarization curves and EIS results show that UNH_2-TENG may offer worthful cathodic protection for carbon steel. The current findings offer high-performance and significantly cost-effective strategy for hunting the mechanical energy from environment to use a self-powered setup designed for fruitful metallic protection from corrosion. The demonstrated pathway may introduce a wide-range of potential applications in metallic corrosion without any external electric supply.

CRediT authorship contribution statement

Penghao Zhu: Conceived and designed the research, Collected the data, Performed the analysis, Wrote the manuscript. **Zaka Ullah**: Participated in discussions of the research, Performed the analysis, Modified the manuscript, **Surong Zheng, Zairui Yang**: Collected the data, Performed the analysis, **Shiwei Yu, Shoupu Zhu, Liwei Liu, Aihua He**: provided valuable discussions, **Cunguo Wang**: Supervision, **Qi Li**: Conceived and designed the research, Wrote and modified the manuscript, Supervision.

Declaration of Competing Interest

The authors declare that they have no known competing financial interests or personal relationships that could have appeared to influence the work reported in this paper.

Data Availability

Data will be made available on request.

Acknowledgments

This work was supported by National Natural Science Foundation of China (Grant Nos. 51972330), the Military Commission Logistics Department (Grant Nos. BY117J013), the State Key Program of National Natural Science Foundation of China (Grant No. 61734008), the Major Scientific and Technological Innovation Project of Shandong Province (Grant No. 2021CXGC010901), and the Natural Science Foundation of Jiangsu Province (Grant No. BK20210129). The authors are grateful to Platforms of Characterization & Test, Collaborative Innovation Center of Suzhou Nano Science and Technology, and Nanofabrication Facility from Suzhou Institute of Nano-Tech and Nano-Bionics, for their technical support and provision of experimental facilities.

Appendix A. Supporting information

Supplementary data associated with this article can be found in the online version at doi:10.1016/j.nanoen.2023.108195.

References

[1] K. Thongchaivetcharat, S. Salaluk, D. Crespy, H. Therien-Aubin, K. Landfester, Responsive colloidosomes with triple function for anticorrosion (Page), ACS Appl. Mater. Interfaces 12 (2020), https://doi.org/10.1021/acsami.0c11866.
[2] Y.Y. Bu, J.P. Ao, A review on photoelectrochemical cathodic protection semiconductor thin films for metals (Page), Green. Energy Environ. 2 (2017), https://doi.org/10.1016/j.gee.2017.02.003.
[3] A.E. Danon, O. Muransky, I. Karatchevtseva, Z. Zhang, Z.J. Li, N. Scales, J.J. Kruzic, L. Edwards, Molten salt corrosion (FLiNaK) of a Ni-Mo-Cr alloy and its welds for application in energy-generation and energy-storage systems (Page), Corros. Sci. 164 (2020), https://doi.org/10.1016/j.corsci.2019.108306.
[4] R. Ding, S. Chen, N. Zhou, Y. Zheng, B.-j Li, T.-j Gui, X. Wang, W.-h Li, H.-b Yu, H.-w Tian, The diffusion-dynamical and electrochemical effect mechanism of oriented magnetic graphene on zinc-rich coatings and the electrodynamics and quantum mechanics mechanism of electron conduction in graphene zinc-rich coatings (Page), J. Alloy. Compd. 784 (2019), https://doi.org/10.1016/j.jallcom.2019.01.070.
[5] M. Fukumoto, C. Tachikawame, Y. Matsuzaka, M. Hara, Formation of Si diffusion layer on stainless steels and their high temperature corrosion resistance in molten salt (Page), Corros. Sci. 56 (2012), https://doi.org/10.1016/j.corsci.2011.11.015.
[6] A. Kalendova, D. Vesely, I. Sapurina, J. Stejskal, Anticorrosion efficiency of organic coatings depending on the pigment volume concentration of polyaniline phosphate (Page), Prog. Org. Coat. 63 (2008), https://doi.org/10.1016/j.porgcoat.2008.06.005.
[7] S.J. Kim, M. Okido, K.M. Moon, An electrochemical study of cathodic protection of steel used for marine structures (Page), Korean J. Chem. Eng. 20 (2003), https://doi.org/10.1007/bf02705566.
[8] X.K. Liu, X. Xu, F.J. Zhang, X.C. Ge, H.F. Ji, Y.Q. Li, S.R. Lu, Z. Wen, A synergistic anti-corrosion system based on durable superhydrophobic F-SiO2/epoxy coatings and self-powered cathodic protection, J. Mater. Chem. A 10 (2022) https://doi.ori./10.1039/D2TA05071D.
[9] L. Bertolini, F. Bolzoni, P. Pedeferri, L. Lazzari, T. Pastore, Cathodic protection and cathodic prevention in concrete: principles and applications (Page), J. Appl. Electrochem. 28 (1998), https://doi.org/10.1023/a:1003404428827.
[10] F. Delfani, N. Rahbar, C. Aghanajafi, A. Heydari, A. KhalesiDoost, Utilization of thermoelectric technology in converting waste heat into electrical power required by an impressed current cathodic protection system (Page), Appl. Energy 302 (2021), https://doi.org/10.1016/j.apenergy.2021.117561.
[11] F.-R. Fan, L. Lin, G. Zhu, W. Wu, R. Zhang, Z.L. Wang, Transparent triboelectric nanogenerators and self-powered pressure sensors based on micropatterned plastic films (Page), Nano Lett. 12 (2012), https://doi.org/10.1021/nl300988z.
[12] F.-R. Fan, Z.-Q. Tian, Z.L. Wang, Flexible triboelectric generator (Page), Nano Energy 1 (2012), https://doi.org/10.1016/j.nanoen.2012.01.004.
[13] Y. Qin, X. Wang, Z.L. Wang, Microfibre–nanowire hybrid structure for energy scavenging (Page), Nature 451 (2008), https://doi.org/10.1038/nature07628.
[14] Z.L. Wang, J.H. Song, Piezoelectric nanogenerators based on zinc oxide nanowire arrays (Page), Science 312 (2006), https://doi.org/10.1126/science.1124005.
[15] G. Zhu, J. Chen, T.J. Zhang, Q.S. Jing, Z.L. Wang, Radial-arrayed rotary electrification for high performance triboelectric generator (Page), Nat. Commun. 5 (2014), https://doi.org/10.1038/ncomms4426.
[16] Y.H. Tsao, R.A. Husain, Y.J. Lin, I. Khan, S.W. Chen, Z.H. Lin, A self-powered mercury ion nanosensor based on the thermoelectric effect and chemical transformation mechanism (Page), Nano Energy 62 (2019), https://doi.org/10.1016/j.nanoen.2019.05.032.
[17] S.H. Wang, L. Lin, Z.L. Wang, Nanoscale triboelectric-effect-enabled energy conversion for sustainably powering portable electronics (Page), Nano Lett. 12 (2012), https://doi.org/10.1021/nl303573d.
[18] Y. Yang, G. Zhu, H.L. Zhang, J. Chen, X.D. Zhong, Z.H. Lin, Y.J. Su, P. Bai, X. N. Wen, Z.L. Wang, Triboelectric nanogenerator for harvesting wind energy and as self-powered wind vector sensor system (Page), ACS Nano 7 (2013), https://doi.org/10.1021/nn4043157.
[19] G. Zhu, Z.H. Lin, Q.S. Jing, P. Bai, C.F. Pan, Y. Yang, Y.S. Zhou, Z.L. Wang, Toward large-scale energy harvesting by a nanoparticle-enhanced triboelectric nanogenerator (Page), Nano Lett. 13 (2013), https://doi.org/10.1021/nl4001053.
[20] K.Q. Xia, Z.Y. Zhu, H.Z. Zhang, C.L. Du, Z.W. Xu, R.J. Wang, Painting a high-output triboelectric nanogenerator on paper for harvesting energy from human body motion (Page), Nano Energy 50 (2018), https://doi.org/10.1016/j.nanoen.2018.06.019.
[21] K.Q. Xia, J.M. Fu, Z.W. Xu, Multiple-frequency high-output triboelectric nanogenerator based on a water balloon for all-weather water wave energy harvesting (Page), Adv. Energy Mater. 10 (2020), https://doi.org/10.1002/aenm.202000426.
[22] A. Goyal, E.K. Olorunnipa, H.S. Pouya, E. Ganjian, A.O. Olubanwo, Potential and current distribution across different layers of reinforcement in reinforced concrete cathodic protection system- a numerical study (Page), Constr. Build. Mater. 262 (2020), https://doi.org/10.1016/j.conbuildmat.2020.120580.
[23] J.J. Shao, M. Willatzen, Z.L. Wang, Theoretical modeling of triboelectric nanogenerators (TENGs) (Page), J. Appl. Phys. 128 (2020), https://doi.org/10.1063/5.0020961.
[24] Y.K. Liu, W.L. Liu, Z. Wang, W.C. He, Q. Tang, Y. Xi, X. Wang, H.Y. Guo, C.G. Hu, Quantifying contact status and the air-breakdown model of charge-excitation triboelectric nanogenerators to maximize charge density (Page), Nat. Commun. 11 (2020), https://doi.org/10.1038/s41467-020-15368-9.
[25] K.Q. Xia, D. Wu, J.M. Fu, N.A. Hoque, Y. Ye, Z.W. Xu, A high-output triboelectric nanogenerator based on nickel-copper bimetallic hydroxide nanowrinkles for self-powered wearable electronics (Page), J. Mater. Chem. A 48 (2020), https://doi.org/10.1039/D0TA09440D.
[26] Z.L. Yin, Y.L. Liu, S.H. Zhou, Z. Yang, W.B. Yang, Constructing zirconium based metal-organic frameworks based electrically-driven self-cleaning membrane for removal of tetracycline: effect of ligand substitution (Page), Chem. Eng. J. 450 (2022), https://doi.org/10.1016/j.cej.2022.138100.
[27] Y. Song, X.L. Cheng, H.T. Chen, J.H. Huang, X.X. Chen, M.D. Han, Z.M. Su, B. Meng, Z.J. Song, H.X. Zhang, Integrated self-charging power unit with flexible supercapacitor and triboelectric nanogenerator (Page), J. Mater. Chem. A 37 (2016), https://doi.org/10.1039/C6TA05816G.
[28] X.-W. Zhang, G.-Z. Li, G.-G. Wang, J.-L. Tian, Y.-L. Liu, D.-M. Ye, Z. Liu, H.-Y. Zhang, J.-C. Han, Engineering, High-performance triboelectric nanogenerator with double-surface shape-complementary microstructures prepared by using simple sandpaper templates (Page), ACS Sustain. Chem. 6 (2018), https://doi.org/10.1021/acssuschemeng.7b03745.

[29] C.J. Lee, A.Y. Choi, J. Park, C. Choi, H.J. Sim, S.J. Kim, Y.T. Kim, Triboelectric generator for wearable devices fabricated using a casting method (vol 6, pg 10094, 2016). RSC Adv. 6 (2016) Page, https://doi.org/10.1039/c6ra90010k.

[30] Y.J. Fan, X.S. Meng, H.Y. Li, S.Y. Kuang, L. Zhang, Y. Wu, Z.L. Wang, G. Zhu, Stretchable porous carbon nanotube-elastomer hybrid nanocomposite for harvesting mechanical energy (Page), Adv. Mater. 29 (2017), https://doi.org/10.1002/adma.201603115.

[31] M. Wang, N. Zhang, Y.J. Tang, H. Zhang, C. Ning, L. Tian, W.H. Li, J.H. Zhang, Y. C. Mao, E.J. Liang, Single-electrode triboelectric nanogenerators based on sponge-like porous PTFE thin films for mechanical energy harvesting and self-powered electronics (Page), J. Mater. Chem. A 5 (2017), https://doi.org/10.1039/c7ta02680c.

[32] Z.C. Qian, R. Li, J. Guo, Z. Wang, X.F. Li, C.C. Li, N. Zhao, J. Xu, Triboelectric nanogenerators made of polybenzazole aerogels as fire-resistant negative tribo-materials (Page), Nano Energy 64 (2019), https://doi.org/10.1016/j.nanoen.2019.103900.

[33] G. Khandelwal, A. Chandrasekhar, N. Raj, S.J. Kim, Metal-organic framework: a novel material for triboelectric nanogenerator-based self-powered sensors and systems (Page), Adv. Energy Mater. 9 (2019), https://doi.org/10.1002/aenm.201803581.

[34] X. Cui, Flat band potential of semiconductor electrodes (Page), Chemistry 80 (2017), https://doi.org/10.14159/j.cnki.0441-3776.2017.12.014.